Dual-mode phase and fluorescence imaging with a confocal laser scanning microscope

Article · November 2018

CITATIONS
0

READS
331

4 authors, including:

Juanjuan Zheng
Xidian University
24 PUBLICATIONS **437** CITATIONS
SEE PROFILE

Chao Zuo
Nanjing University of Science and Technology
380 PUBLICATIONS **6,889** CITATIONS
SEE PROFILE

Peng Gao
KIT, Germany
54 PUBLICATIONS **678** CITATIONS
SEE PROFILE

Optics Letters

Dual-mode phase and fluorescence imaging with a confocal laser scanning microscope

JUANJUAN ZHENG,[3] CHAO ZUO,[4] PENG GAO,[1,2] AND G. ULRICH NIENHAUS[1,2,5,6,*]

[1]Institute of Applied Physics, Karlsruhe Institute of Technology, 76128 Karlsruhe, Germany
[2]Institute of Nanotechnology, Karlsruhe Institute of Technology, 76344 Eggenstein-Leopoldshafen, Germany
[3]School of Physics and Optoelectronic Engineering, Xidian University, 710071 Xi'an, China
[4]School of Electronic and Optical Engineering, Nanjing University of Science and Technology, 210094 Nanjing, China
[5]Institute of Toxicology and Genetics, Karlsruhe Institute of Technology, 76344 Eggenstein-Leopoldshafen, Germany
[6]Department of Physics, University of Illinois at Urbana-Champaign, Urbana, Illinois 61801, USA
*Corresponding author: uli@uiuc.edu

Received 16 October 2018; accepted 19 October 2018; posted 23 October 2018 (Doc. ID 348365); published 15 November 2018

We present dual-mode phase and fluorescence imaging in a confocal laser scanning microscopy (CLSM) system. For phase imaging, the depth of field of the CLSM system is extended by fast axial scanning with a tunable acoustic gradient index of refraction lens. Under transillumination, intensity images of the sample are recorded at a few different defocusing distances. The phase image is reconstructed from these intensity images by using the transport-of-intensity equation. The 3D fluorescence image is obtained by confocal scanning. The dual-mode images with pixel-to-pixel correspondence yield complementary quantitative structural and functional information. Combination of the two imaging modalities enables standalone determination of the refractive index of live cells.

https://doi.org/10.1364/OL.43.005689

Being minimally invasive to cells or tissues, quantitative phase microscopy (QPM) [1–4] and fluorescence microscopy (FM)[5] are often-used techniques to visualize biological cells with high contrast. QPM is label free and provides high-contrast phase images by exploiting wavefront changes induced by optical path length (OPL) variations resulting from changes in the refractive index (RI) or thickness of cells. There are many approaches to quantitative phase imaging, e.g., digital holographic microscopy [1–3], wavefront sensors [6,7], reference-less phase retrieval based on the transport-of-intensity equation (TIE) method [8,9], and iterative phase retrieval [10,11]. However, all of these approaches rely on wide-field detection, and consequently lack sectioning capability. Depth-resolved tomographic imaging can be realized by using partially coherent light, tunable illumination wavelength or angle, and sample rotation [12]. This technique, however, requires a complicated imaging system and elaborate data acquisition and reconstruction.

FM enables visualization of selected cellular structures using specific labeling with fluorophores [13–15]. 3D sectioning can be realized by structured illumination using periodic line patterns [16], light sheet illumination [17,18], which confines the observation to the neighborhood of the focal plane, or by scanning the sample point by point with a focused spot in combination with out-of-focus light rejection by a pinhole mask using a confocal laser scanning microscope (CLSM) [19–21].

In biomedical imaging, there is an emerging trend to combine different imaging modalities so as to extract not only more but complementary data from one and the same sample. For example, colocalized functional structures of the cell interior can be obtained by FM contoured with the phase image. The combination of QPM and FM enables measurement of the RI of cells or tissues. However, efforts to measure the RI of live cells have been impeded by the need to simultaneously measure the thickness h and the phase $\Delta\varphi$ of the same cell. Multiple indirect approaches have been developed to determine h and $\Delta\varphi$ simultaneously by rotating the illumination beam [22], using dual-wavelength illumination [23] or air bubbles [24]. Alternatively, the combination of confocal microscopy with wide-field QPM was used to separately measure h by CLSM and $\Delta\varphi$ [25] by wide-field QPM. However, it is nontrivial to accurately overlay the two channels with exact pixel-to-pixel correspondence in light of image distortion and varying pixel sizes between the two images. Combination of phase and fluorescence dual-mode imaging in a wide-field microscope has also been performed by using spatial frequency multiplexing [26,27].

The limited depth of field (DOF) CLSM precludes TIE-based phase retrieval. Here, we extend the DOF of CLSM sixfold by axial scanning with a tunable acoustic gradient index of refraction (TAG) lens to enable application of the TIE method in a CLSM system. The combination of fluorescence and phase imaging provides an elegant way to determine the RI of live cells.

Our dual-mode CLSM setup (Fig. 1) is built around an inverted microscope frame (DMi8, Leica Microsystems, Mannheim, Germany). For fluorescence imaging, a 640-nm diode laser (LDH-P-C-640B; PicoQuant, Berlin, Germany) is used for excitation. After being reflected by a quad-band dichroic mirror (zt 405/473/561/640 RPC, AFH, Tübingen, Germany), the 640-nm light is passed through a TAG lens (model 2.0, TAG Optics, Princeton, NJ) and focused onto

the sample by a water immersion objective (HCX PL APO W CORR CS 63 × /1.2, Leica). The TAG lens allows resonant axial scanning of the excitation focus over several micrometers at a frequency of 147 kHz. The transmitted light or the sample fluorescence passes through the dichroic mirror and is coupled into a multi-mode fiber serving as a pinhole of 1 AU (for 640-nm light). Subsequently, only the fluorescence, but not the transmitted light, is filtered by a band-pass filter (HC 676/37, Semrock, Rochester, US), and counted by an avalanche photodiode (τ-SPAD, Single Photon Counting Module, PicoQuant, Berlin, Germany). A 2D galvanometer scanner located in the conjugate plane of the rear aperture of the objective [not included in Fig. 1(a)] allows lateral scanning of the sample. A piezo actuator (P-720, Physik Instrumente, Karlsruhe, Germany) with an accuracy of 0.5 nm in combination with a motorized linear actuator (Leica) enables slow scanning over a wide axial range. As an example, we show a 3D fluorescence image of membrane-stained HeLa cells in Fig. 1(b) and the corresponding optical path difference (OPD $= \varphi/k$; $k = 2\pi/\lambda$) image in Fig. 1(c).

For QPM imaging, we illuminate the sample from the top using the mercury arc source (HXP R120/45C, OSRAM, Munich, Germany) of the microscope frame, filtered with a band-pass (center wavelength/bandwidth, 510/10 nm). The numerical aperture (NA) of the illumination optics is <10% of the NA of the imaging objective to ensure a certain degree of spatial coherence to achieve high phase contrast upon defocusing [28]. Our CLSM has an axial sectioning depth of 0.9 ± 0.1 μm, as determined by measuring the axial extension of the focus [Fig. 2(a), left]. When the TAG lens is turned on, the focus moves roughly sinusoidally in the axial direction. The scanning period of 6.80 μs is much shorter than the pixel/voxel dwell time of 40 μs, so that the focus appears to be extended [Fig. 2(a), right]. The intensity distributions along the axial direction [Figs. 2(b) and 2(c)] reveal that the axial width of the focus is extended to 6.1 ± 0.3 μm when using the 63× objective. With a 20× objective (HC PL APO 20 × /0.75 IMM CORR CS2, Leica), the axial width of the focus is extended from 7.7 ± 0.8 μm to 41 ± 4 μm. Here we define the axial width as the distance for which the intensity has dropped to

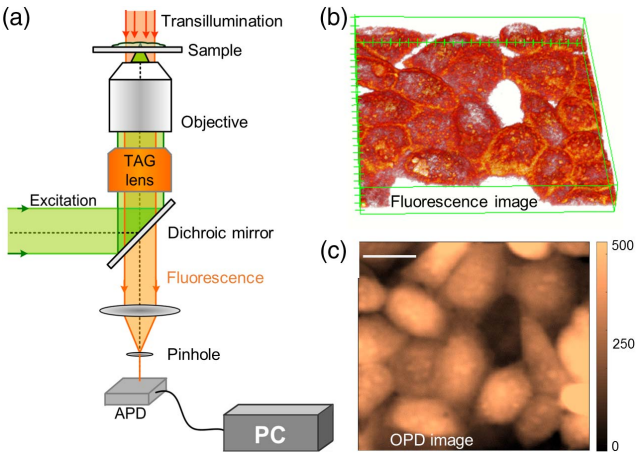

Fig. 1. Dual-mode fluorescence and phase imaging in a CLSM system. (a) Schematic depiction of the CLSM; (b) exemplary fluorescence; and (c) optical path difference (OPD) images measured with this setup. Scale bar, 20 μm; color bar labels, nm.

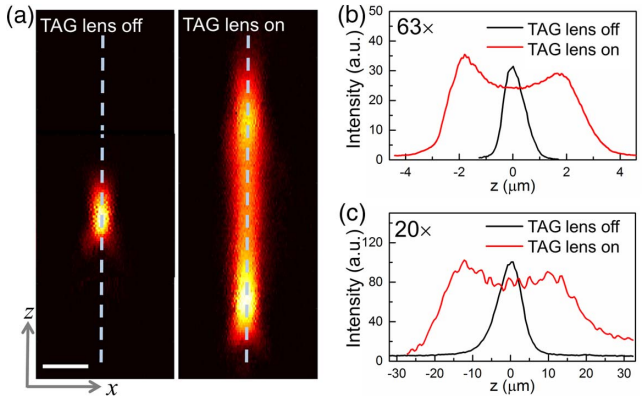

Fig. 2. Characterization of the axial focus extension of our CLSM system with and without TAG lens turned on by 3D imaging of an 80-nm diameter gold bead (EM.GC80, BBI solutions, Cardiff, UK). (a) xz section of the focus with the TAG lens off (left) and on (right); scale bar, 1 μm. (b) Intensity profiles along the dashed lines in (a), using objectives with magnifications (b) 63× (scanned volume $3 \times 3 \times 12$ μm^3) and (c) 20× (scanned volume $3 \times 3 \times 70$ μm^3).

$1/e^2$ of the maximum intensity. In conventional wide-field QPM, samples are taken to be optically thin, and the phase is calculated simply by integration of the OPL through the sample along the optical axis. The scattering due to internal structures of the sample from different planes is averaged. The final intensity image is the sum of transmitted light and average scattered light. To retrieve the phase of the sample with the TIE [8], three intensity images are recorded, one in focus and two defocused by $\pm\Delta z$. The differences among the three intensity images result solely from defocusing of the transmitted light. If we record the three intensity images with a CLSM, the transmitted light is recorded in the same way as with a wide-field setup, whereas scattered light is collected only from the in-focus plane and thus is different for the three intensity images. Consequently, the presence of the sectioned scattered light prevents us from using the TIE in standard CLSM systems. However, if the axial focus extension, i.e., the sectioning depth of the CLSM, can be increased by more than twofold, the scattered light in the three intensity images separated by the sectioning depth will be identical and, thus, TIE-based phase imaging with a CLSM becomes feasible.

In the implementation, three intensity images of a sample are recorded by moving the objective to three positions $m\Delta z$, with $m = -1, 0, 1$. We denote the images recorded in the three planes as $I_{-\Delta z}(x,y)$, $I_0(x,y)$, $I_{\Delta z}(x,y)$. The intensity derivative along the optical axis can be approximated by

$$\frac{\partial I}{\partial z} = \frac{I_{\Delta z} - I_{-\Delta z}}{2\Delta z}. \tag{1}$$

Together with the in-focus image I_0, the phase can be retrieved by solving the TIE [8,9]:

$$-k\frac{\partial I}{\partial z} = \nabla \cdot (I_0 \nabla \varphi_0), \tag{2}$$

with wavenumber $k = 2\pi/\lambda$, λ being the center wavelength of the transillumination beam; ∇ represents the del operator. By introducing an auxiliary function Ψ satisfying $\nabla\Psi = I_0\nabla\varphi_0$, Eq. (2) can be converted to a Poisson equation:

$$-k\frac{\partial I}{\partial z} = \nabla^2\Psi. \quad (3)$$

Equation (3) can be solved for Ψ with a fast discrete cosine transform (DCT)-based algorithm under homogeneous Neumann boundary conditions [29]. Then, by plugging $\nabla\Psi = I_0\nabla\varphi_0$ into Eq. (2), we can generate a second Poisson equation:

$$\nabla\cdot(I_0^{-1}\nabla\Psi) = \nabla^2\varphi_0. \quad (4)$$

Equation (4) can also be solved for φ_0 with the DCT-based algorithm. Thus, apart from an arbitrary additive constant irrelevant for QPM, the phase can be uniquely determined and converted to an OPD $= \varphi_0/k$. Notably, Δz should be small enough to satisfy the approximation made in Eq. (1). Another TIE-based iterative algorithm [30] takes into account high-order derivatives of the intensity. It provides more accurate phase reconstruction by recording more intensity images over a larger axial range.

We tested dual-mode imaging with our CLSM by using human cervical cancer HeLa cells (LGC Standards GmbH, Wesel, Germany), cultured in Dulbecco's modified Eagle's medium (DMEM), and human lung cancer NCI-H1703 cells, cultured in Roswell Park Memorial Institute medium (RPMI) containing 10% fetal bovine serum (FBS, Thermo Fischer Scientific). The cells were seeded on eight-well Lab-Tek II chambered coverglass (Thermo Fischer Scientific) and cultured for 24 h at 37°C and 5% CO_2. Subsequently, the cells were labeled with CellMask Deep Red plasma membrane stain (Thermo Fischer Scientific) added to the culture medium for 5 min. Before imaging, the cells were thoroughly washed twice with phosphate buffered saline (PBS), and fresh culture medium was added to the cell chambers. The RI of DMEM was determined with a refractometer (PAL-RI, ATAGO, Tokyo, Japan) as $n_{\text{medium}} = 1.3372$. For phase imaging of NCI-H1703 cells, nine intensity images (256×256 pixels, 470×470 nm^2) were recorded under transillumination from $z = -8$ to 8 μm in steps of 2 μm [Fig. 3(a)]. The pixel dwell time was set to 40 μs. For each slice, four frames were averaged. Apparently, the contrast of the cells is minimal in the in-focus plane. By using the three intensity images with $z = -2$, 0, 2 μm, the OPD image of the sample was reconstructed with Eqs. (2)–(4), as shown in Fig. 3(b). In addition, all nine intensity images were used to reconstruct the OPD with the algorithm based on higher-order intensity derivatives [Fig. 3(c)] [30]. Comparison of Figs. 3(b) and 3(c) reveals that both methods provide similar results, although the latter one has fewer artifacts (slow phase variation) in regions between cells. The black spots in Figs. 3(b) and 3(c) are intrinsic artifacts caused by the use of periodic boundary conditions in the TIE-based approach. Such artifacts can be avoided by placing a rectangular aperture in the intermediate image plane of the microscope and using Neumann boundary conditions [29].

For 3D FM imaging, the TAG lens was turned off, and a volume of 110 μm × 110 μm × 20 μm^3 in Fig. 4(a) shows orthogonal views of the 3D image with high contrast. To determine the axial thickness, $h(x,y)$, of the cells, we go through the image stack from top to bottom [Fig. 4(c)] for all xy pixels, and search for the first axial position z for which the intensity satisfies $I_z(x,y) > I_{\text{mem}}/2$, defining the top of the cell. Here, I_{mem} is the average intensity of the cell membrane obtained by locating the right peak of the bimodal intensity histogram. For this purpose, a histogram is generated with the voxelated intensities of the 3D image. Since the cells are adherent to the culture dish, their bottom can be determined simply by searching for the frame with the maximal number of pixels satisfying $I_z(x,y) > I_{\text{mem}}/10$. The z position corresponding to the bottom of the cells is subtracted to yield the offset-corrected thickness image $h_o(x,y)$ shown in Fig. 4(b). The RI of the cells can be determined if both a 3D image (FM) and an OPD image (QPM), have been measured. Generally, for a cell with average RI, n_{cell}, along the light path, suspended in a medium with RI, n_{medium}, the OPD of light of wavelength λ passing through the cell with respect to the medium is

$$\text{OPD}(x,y) = \Delta n\, h(x,y), \quad (5)$$

with $\Delta n = n_{\text{cell}} - n_{\text{medium}}$. Figures 5(a) and 5(b) show $h_o(x,y)$ of the cells from 3D FM and OPD(x,y) from TIE-based QPM, respectively. Then, the average RI difference, $\Delta n(x,y)$, can be calculated with Eq. (5), as displayed in Fig. 5(c). For quantitative evaluation, $h_o(x,y)$, OPD(x,y), and $\Delta n(x,y)$ were analyzed along the dashed lines in Figs. 5(a)–5(c). Both $h_o(x,y)$ and OPD(x,y) look similar [Fig. 5(d)]; deviations at the cell edge are artifacts introduced by the TIE-based method [9].

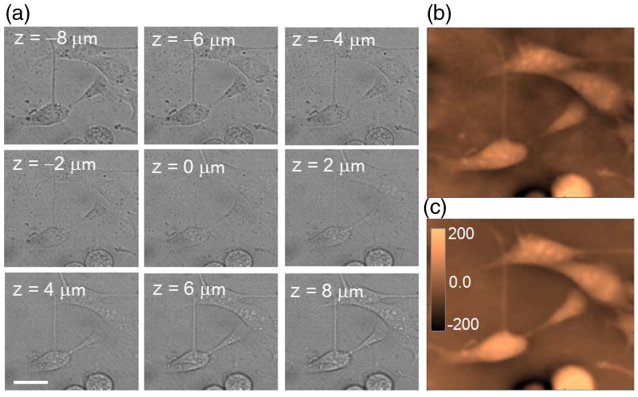

Fig. 3. Phase imaging of NCI-H1703 cells. (a) Axial stack of intensity images from $z = -8$ to 8 μm in steps of 2 μm; scale bar, 30 μm. OPD images reconstructed by using (b) Eqs. (2)–(4) and (c) higher-order intensity derivatives [30]; color bar labels, nm.

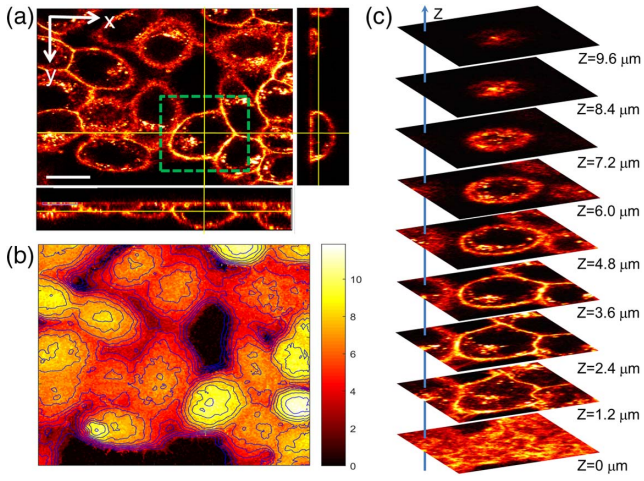

Fig. 4. 3D fluorescence imaging of plasma membrane-stained HeLa cells. (a) Orthogonal views of the cells; scale bar, 20 μm; (b) contour map of the thickness of cells with 1-μm line separation; (c) 3D image stack of the region marked by the dashed rectangle in (a).

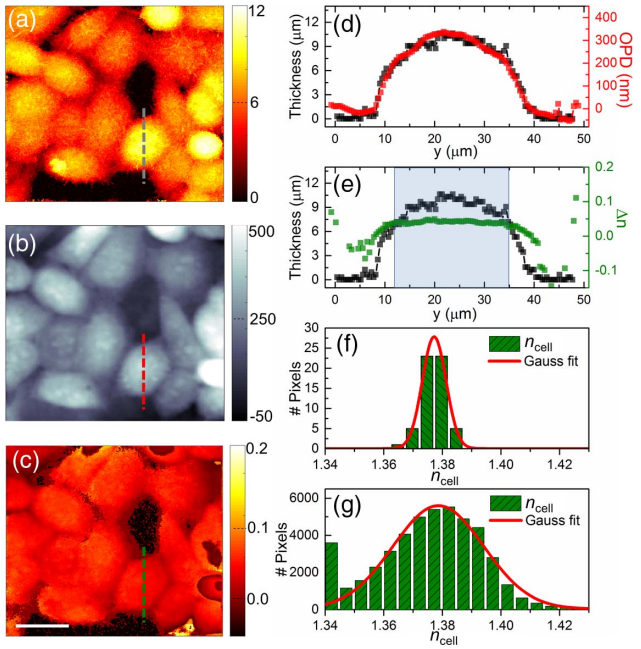

Fig. 5. RI determination on HeLa cells. (a) Thickness (μm), (b) OPD (nm), and (c) Δn images of the cells; scale bar, 20 μm. (d) Thickness (black) and OPD (red) distributions along the dashed line in (a) and (b). (e) Thickness (black) and Δn (green) distributions along the same line in (c); histograms of the number of pixels as a function of n_{cell}, bin width 0.005, from (f) pixels in the region shaded in light blue in (e), and (g) pixels with $h > 6$ μm in (c).

Furthermore, Δn in Fig. 5(e) is constant in the central part of the cell ($h > 6$ μm) and varies at the cell edges. The average RI of the cell can be calculated by adding n_{medium} to Δn. The statistics of n_{cell} from the part with $h > 6$ μm on the selected line [Fig. 5(f)] yields $n_{cell} = 1.377 \pm 0.005$ (mean ± half width at half maximum (HWHM) from a Gaussian fit). Moreover, the statistics of n_{cell} over the whole image (but keeping the constraint $h(x, y) > 6$ μm) [Fig. 5(g)] yields $n_{cell} = 1.378 \pm 0.018$ (mean ± HWHM). Interestingly, the error from the statistics over the image is considerably larger than the statistics over the line. This is mainly due to the heterogeneous RI distribution within a cell and deviations between different cells. The result agrees very well with previously reported RIs, 1.33–1.37 of HeLa cells [25], 1.39 ± 0.01 [31] for HeLa cells suspended in PBS-glycerol, and 1.38–1.41 for a number of tissue types [32].

In summary, we have implemented dual-mode phase and fluorescence imaging with strict pixel-to-pixel correspondence in a CLSM. Combining phase and 3D fluorescence data allowed us to determine the RI of HeLa cells. Phase imaging can track morphological changes in cells such as cell type/cell cycle/substrate-dependent growth and division, drug-induced shear stress, or hydration level. Fluorescence imaging can probe subcellular structures and molecular interactions via specific labeling. Therefore, the two imaging modes yield complementary information that can help unravel complex biological processes where both morphological and functional information is needed.

Next, we will implement simultaneous dual-mode 3D imaging using two different colors for FM and QPM and time-correlated single-photon counting (TCSPC) to tag each photon with its arrival time and the trigger signal from the TAG lens. The mutual time difference can then be used for axial position determination to achieve ultrafast 3D imaging.

Funding. Helmholtz Association; National Natural Science Foundation of China (NSFC) (61475187, 61575154, 61605150); China Postdoctoral Science Foundation (2017M610623).

REFERENCES

1. E. Cuche, P. Marquet, and C. Depeursinge, Appl. Opt. **38**, 6994 (1999).
2. P. Ferraro, G. Coppola, S. De Nicola, A. Finizio, and G. Pierattini, Opt. Lett. **28**, 1257 (2003).
3. Y. Park, G. Popescu, K. Badizadegan, R. R. Dasari, and M. S. Feld, Opt. Lett. **32**, 811 (2007).
4. P. Gao, G. Pedrini, and W. Osten, Opt. Lett. **38**, 1328 (2013).
5. U. Kubitscheck, *Fluorescence Microscopy: From Principles to Biological Applications*, 2nd ed. (Wiley-VCH, 2017).
6. B. C. Platt and R. Shack, J. Refract. Surg. **17**, S573 (2001).
7. R. Ragazzoni, J. Mod. Opt. **43**, 289 (1996).
8. M. R. Teague, J. Opt. Soc. Am. **73**, 1434 (1983).
9. C. Zuo, Q. Chen, Y. Yu, and A. Asundi, Opt. Express **21**, 5346 (2013).
10. J. R. Fienup, Appl. Opt. **21**, 2758 (1982).
11. P. Gao, G. Pedrini, C. Zuo, and W. Osten, Opt. Lett. **39**, 3615 (2014).
12. W. Choi, C. Fang-Yen, K. Badizadegan, S. Oh, N. Lue, R. R. Dasari, and M. S. Feld, Nat. Methods **4**, 717 (2007).
13. K. Nienhaus and G. U. Nienhaus, J. Mol. Biol. **428**, 308 (2016).
14. E. Betzig, G. H. Patterson, R. Sougrat, O. W. Lindwasser, S. Olenych, J. S. Bonifacino, M. W. Davidson, J. Lippincott-Schwartz, and H. F. Hess, Science **313**, 1642 (2006).
15. P. Gao, B. Prunsche, L. Zhou, K. Nienhaus, and G. U. Nienhaus, Nat. Photonics **11**, 163 (2017).
16. M. G. L. Gustafsson, Proc. Natl. Acad. Sci. USA **102**, 13081 (2005).
17. J. Huisken, J. Swoger, F. Del Bene, J. Wittbrodt, and E. H. K. Stelzer, Science **305**, 1007 (2004).
18. A. Y. Kobitski, J. C. Otte, M. Takamiya, B. Schafer, J. Mertes, J. Stegmaier, S. Rastegar, F. Rindone, V. Hartmann, R. Stotzka, A. Garcia, J. van Wezel, R. Mikut, U. Strähle, and G. U. Nienhaus, Sci. Rep. **5**, 8601 (2015).
19. C. J. R. Sheppard and R. Kompfner, Appl. Opt. **17**, 2879 (1978).
20. M. Gu, T. Tannous, and J. R. Sheppard, Opt. Lett. **21**, 312 (1996).
21. M. A. A. Neil, R. Juskaitis, and T. Wilson, Opt. Lett. **22**, 1905 (1997).
22. F. Charrière, A. Marian, F. Montfort, J. Kuehn, T. Colomb, E. Cuche, P. Marquet, and C. Depeursinge, Opt. Lett. **31**, 178 (2006).
23. B. Rappaz, F. Charriere, C. Depeursinge, P. J. Magistretti, and P. Marquet, Opt. Lett. **33**, 744 (2008).
24. B. Kemper, D. Carl, J. Schnekenburger, I. Bredebusch, M. Schafer, W. Domschke, and G. von Bally, J. Biomed. Opt. **11**, 34005 (2006).
25. C. L. Curl, C. J. Bellair, T. Harris, B. E. Allman, P. J. Harris, A. G. Stewart, A. Roberts, K. A. Nugent, and L. M. D. Delbridge, Cytometry Part A **65A**, 88 (2005).
26. S. Chowdhury, W. J. Eldridge, A. Wax, and J. A. Izatt, Opt. Lett. **40**, 4839 (2015).
27. Y. N. Nygate, G. Singh, I. Barnea, and N. T. Shaked, Opt. Lett. **43**, 2587 (2018).
28. E. D. Barone-Nugent, A. Barty, and K. A. Nugent, J. Microsc. **206**, 194 (2002).
29. C. Zuo, Q. Chen, H. R. Li, W. J. Qu, and A. Asundi, Opt. Express **22**, 18310 (2014).
30. L. Waller, L. Tian, and G. Barbastathis, Opt. Express **18**, 12552 (2010).
31. J. J. Zheng, P. Gao, X. P. Shao, and G. U. Nienhaus, Appl. Opt. **56**, 9000 (2017).
32. F. P. Bolin, L. E. Preuss, R. C. Taylor, and R. J. Ference, Appl. Opt. **28**, 2297 (1989).